Spectroscopic Studies of OCS-Doped ^{4}He Clusters with 9−72 Helium Atoms: Observation of Broad Oscillations in the Rotational Moment of Inertia†

A. R. W. McKellar,*,‡ Yunjie Xu,§ and Wolfgang Jäger§

Steacie Institute for Molecular Sciences, National Research Council of Canada, Ottawa, Ontario K1A 0R6, Canada, and Department of Chemistry, University of Alberta, Edmonton, Alberta T6G 2G2, Canada

Received: January 24, 2007; In Final Form: March 20, 2007

High-resolution spectra of He_N−OCS clusters with N up to 39 in the microwave region and up to 72 in the infrared region were observed with apparatus-limited line widths of about 15 kHz and 0.001 cm^{-1}, respectively. The cold (∼0.2 K) clusters were produced in pulsed supersonic jet expansions of very dilute OCS + He mixtures and probed using a microwave Fourier transform spectrometer or a tunable infrared diode laser spectrometer. Consistent analyses of the microwave and infrared data yield band origins for the carbonyl stretching vibration, together with rotational parameters for the ground and excited vibrational states. The rotational constant, B, passes through a minimum at $N = 9$ and then rises as the He atoms uncouple from the OCS rotational motion as a result of superfluid effects. There are broad unexpected oscillations in B, with maxima at $N = 24$ and 47 and minima at $N = 36$ and 62. The change in B upon vibrational excitation, which is negative for the OCS molecule, converges to positive values for $N > 15$. These results help to bridge the gap between individual molecules and bulk matter with atom-by-atom resolution over a significant range of cluster sizes.

1. Introduction

Helium nanodroplets[1−3] provide a unique microscopic laboratory for isolating, stabilizing, and investigating novel molecular arrangements, as well as for studying superfluid effects in a finite system. The many applications of nanodroplets have been brilliantly explored in an amazing array of experiments in the laboratory of Roger E. Miller.[4] One aspect of nanodroplet science involves spectroscopic observations of the rotational motion of small molecules in helium nanodroplets, exemplified by vibrational and rotational transitions in the carbonyl sulfide molecule, OCS. Such measurements can constitute an ingenious "microscopic Andronikashvili experiment",[5] analogous to the pioneering measurements[6] of bulk superfluid helium with a torsional oscillator disk. That is, by monitoring the rotational dynamics of an immersed probe, it is possible to directly explore the (super)fluid response in a bulk sample[6] or in a droplet.[5]

Although nanodroplets are indeed small (containing hundreds to thousands of atoms), they cannot generally be produced and detected with specific sizes (e.g., exactly $N = 549$ atoms), nor do they extend in size all the way down to the limit of a few atoms. Recently, it has become possible to bridge part of this gap by directly observing smaller clusters ($N \approx 10$ He atoms) by means of high-resolution microwave and infrared spectroscopy of seeded molecular beams.[7−18] Such experiments, and many related theoretical calculations, now indicate that the onset of superfluid behavior in small clusters can take place with as few as 6−10 helium atoms, depending on the probe molecule.

Carbonyl sulfide is a popular probe molecule for helium cluster studies, in part because it is a strong microwave and infrared chromophore and because its rotational constant B (proportional to the inverse of the moment of inertia) is neither too large nor too small. A variety of experiments[5,7−10,19−21] and calculations[22−27] on the spectroscopy of OCS in He clusters and nanodroplets have been reported. The He−OCS intermolecular potential energy surface[25,28−30] and binary van der Waals complex[10,30−32] are both well-characterized. In this article, we report the detection and assignment of resolved spectra of He_N−OCS clusters all the way to $N = 70$ in the infrared (IR) region and to $N = 39$ in the microwave (MW) region. This wide span of cluster sizes encompasses a significant fraction of the entire range of changes in properties in going from individual molecules to nanodroplets to bulk matter. The observed transitions remain sharp (IR, ∼0.001 cm^{-1}; MW, ∼15 kHz) up to the largest assigned clusters (and possibly beyond), and the derived B values exhibit broad unexpected oscillations as they slowly approach the limiting nanodroplet value. Preliminary results from this work were reported previously;[33] the present article provides further details and supporting evidence.

2. Experimental Methods

The observations were made on pulsed supersonic jet expansions of very dilute mixtures of OCS (<0.01%) in helium, with cooled jet nozzles (as low as −140 °C) and rather high backing pressures (up to 120 atm). The IR measurements were made at the Steacie Institute for Molecular Sciences, Ottawa, Canada, using a tunable diode laser source operating in a rapid-scan signal-averaging mode, as described previously.[9,34] The apparatus was altered to a configuration with two separately pumped vacuum chambers to allow moderate skimming of the jet. This reduces Doppler line broadening and, to some extent, combines the advantages previously described for slit-shaped and pinhole nozzles (narrower lines and increased clustering, respectively). Typical spectra shown here were obtained using a relatively large (8 mm diameter) skimmer opening, with a

† Part of the "Roger E. Miller Memorial Issue".

* To whom correspondence should be addressed. E-mail: robert.mckellar@nrc-cnrc.gc.ca.

‡ National Research Council of Canada.

§ University of Alberta.

10.1021/jp070618w CCC: $37.00
Published on Web 04/25/2007

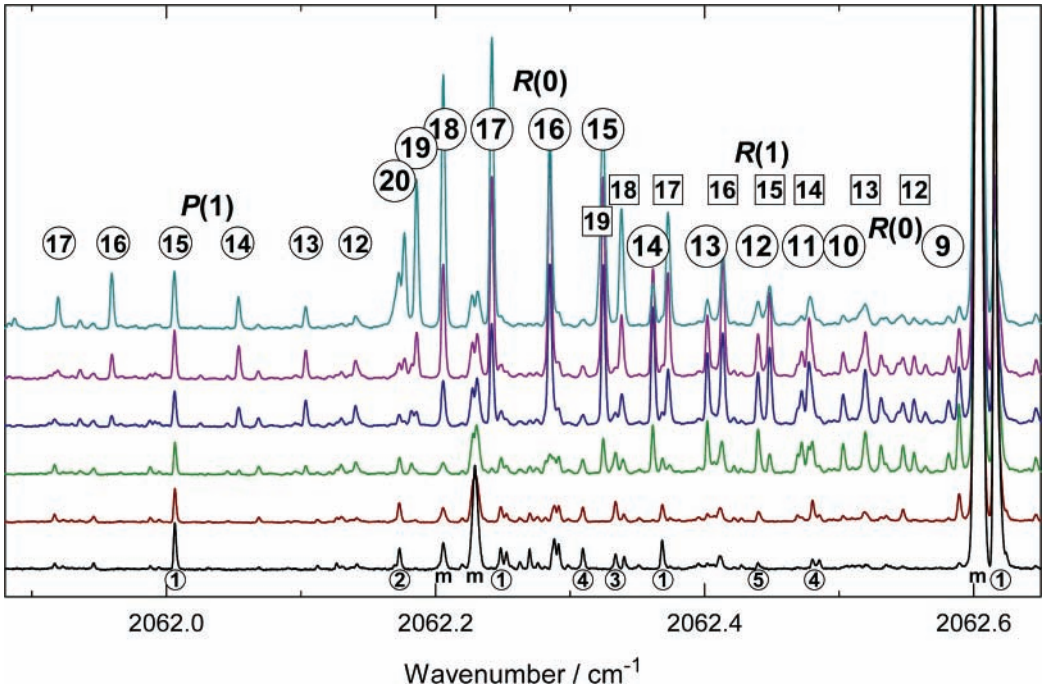

Figure 1. Observed infrared spectra of He_N−OCS clusters, stacked in order of increasing clustering. The jet temperature was −60 °C, and the backing pressure was varied from 7.8 to 23 atm between the bottom and top traces. The numbers below the bottom trace indicate cluster sizes, *N*, for certain transitions of smaller clusters,[9,10,31] and the letter m indicates OCS monomer lines. The numbers above the top trace show the *N* values for the *R*(0) series (large circles), *P*(1) series (small circles), and *R*(1) series (squares). Note that the *R*(0) line for $N = 15$ seems to have extra strength in the top trace because the *R*(1) line for $N = 19$ lies underneath.

skimmer-to-laser beam distance of about 90 mm and nozzle-to-skimmer distances of 3−12 mm. The effective rotational temperature observed in the spectra was found to depend on various experimental factors. Generally, we noted values around 0.2−0.3 K, which is actually colder than the typical temperature (∼0.37 K) in ^{4}He nanodroplet experiments. When the degree of skimming was increased (by using larger nozzle-to-skimmer distances), we found that the effective temperature was increased and the clustering was somewhat reduced. This was presumably due to collisions with atoms backscattered from the skimmer.

The MW measurements were made at the University of Alberta, Edmonton, Alberta, Canada, using a Fourier transform microwave (FTMW) spectrometer[35] that incorporates double-resonance capabilities,[36] now improved by utilizing signal decoherence by resonant pump radiation. In this setup, the pump microwave radiation is radiated using a horn antenna and then propagated through free space to intersect the molecular beam in a perpendicular fashion. The pump radiation power and distance between horn antenna and molecular beam can be adjusted empirically to achieve the largest decoherence effect, i.e., decrease in signal intensity.

Neither spectrometer is able to determine cluster sizes directly. Our assignments of cluster size, *N*, were thus necessarily indirect, made primarily on the basis of the variation in signal strength with jet expansion conditions. That is, lower jet temperatures and higher backing pressures tended to give larger clusters. We also utilized spectral patterns (e.g., the regularity of infrared vibrational shifts) and consistency between IR and MW results.

3. Results

3.1. He_N−OCS Clusters with $N = 9$−20. We previously reported[7−9] spectra of He_N−OCS clusters up to $N = 8$. In this range, the rotational constant, *B*, was found to decrease monotonically from 6082 MHz, the bare OCS molecule value,

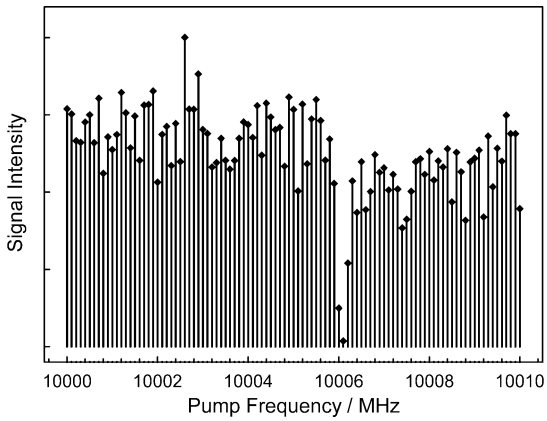

Figure 2. Example of a double-resonance scan. The signal frequency was fixed at 7317.12 MHz, i.e., the transition frequency of the *R*(1) ($J = 2 \leftarrow 1$) transition of the cluster with $N = 12$. The pump frequency was scanned from 9990 to 10100 MHz, and we show a section from 10000 to 10010 MHz, in which the resonance with the *R*(2) ($J = 3 \leftarrow 2$) transition was found at 10006.1 MHz. The signal intensity decreased by a factor of 35 at 10006.1 MHz compared to the average signal intensity, making detection of the double-resonance effect unambiguous. The noise in the double-resonance scan is mainly a result of the pulse-to-pulse fluctuations in the nozzle operation.

to 1448 MHz for He_8−OCS. This is the expected classical behavior, as adding more He atoms "naturally" increases the rotational moment of inertia, which is inversely proportional to *B*. However, we know that the *B* value for OCS in much larger helium nanodroplets (with $N = 10^3$−10^4) is 2194 MHz,[19] considerably larger than 1448 MHz, the $N = 8$ value. It was thus clear by implication that there must be a turnaround in the *B* value somewhere above $N = 8$. This turnaround, which corresponds to the onset of superfluid behavior in the cluster, was subsequently observed in He_N−N_2O clusters[11] at $N = 7$−10 and in He_N−CO_2 clusters[12] at $N = 6$. Calculations had indicated

TABLE 1: Observed Infrared and Microwave Transitions of He_N−OCS Clusters for $N = 12-20$

	infrared transitions (cm^{-1})					microwave transitions[a] (MHz)	
N	$R(0)$	$P(1)$	$R(1)$	$P(2)$	$R(2)$	$R(0)$	$R(1)$
12	2062.4403	2062.1821	2062.5557	2062.0679		3855.7310	7317.1179[b]
13	2062.4021	2062.1406	2062.5202	2062.0254	2062.6103	3910.4600	7393.9369
14	2062.3622	2062.1035	2062.4782	2061.9918	2062.5646	3853.7461	7245.9885
15	2062.3254	2062.0536	2062.4489	2061.9354	2062.5444	4044.3040	7643.7669
16	2062.2856	2062.0061	2062.4138	2061.8829	2062.5169	4160.1618	7902.0085
17	2062.2427	2061.9596	2062.3734	2061.8340	2062.4800	4211.9700	8027.8155
18	2062.2065	2061.9198	2062.3390		2062.4459	4270.5570	8137.7468
19	2062.1861	2061.8876	2062.3244	2061.7531	2062.4377	4462.0031	8518.1
20	2062.1776	2061.8651	2062.3224	2061.7242		4664.3947	8926.7

[a] Linking of each microwave $R(0)/R(1)$ pair listed here was confirmed by double resonance. [b] For $N = 12$, the $R(2)$ microwave transition was also observed at 10006.1 MHz.

TABLE 2: Tentative Assignments of Infrared and Microwave Transitions of He_N−OCS Clusters with $N = 9-11$

	infrared transitions (cm^{-1})			microwave transitions[a] (MHz)		
N	$R(0)$	$P(1)$	$R(1)$	$R(0)$	$R(1)$	$R(2)$
9	2062.5822				5558.2986	8205.0
10	2062.5037	2062.2819		3320.0047	6340.7276	8791.7
11	2062.4729		2062.5822		6908.2738	

[a] For $N = 9$ and 10, the linking of each microwave pair or triplet was confirmed by double resonance.

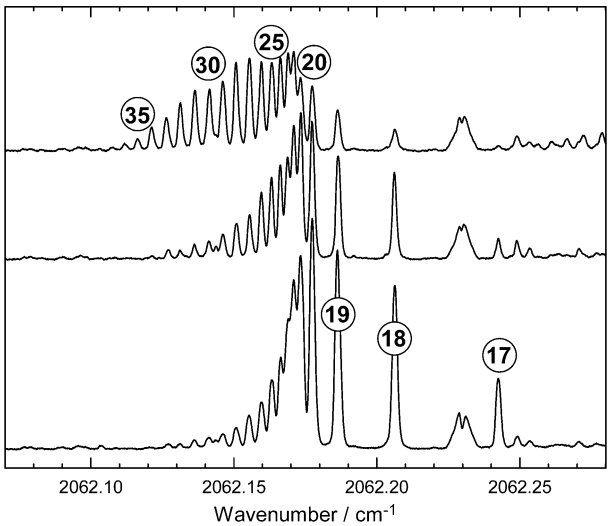

Figure 3. Observed spectra showing the pileup of $R(0)$ transitions around $N = 20$ in the IR spectrum of He_N−OCS clusters, recorded with the skimmer and other experimental conditions optimized for narrow line widths. Jet temperature, −80 °C; backing pressures, 21−27 atm.

that the turnaround for He_N−OCS clusters should occur in the range of $N = 6-9$.[23,24]

Another kind of turnaround was observed for the vibrational shifts in the IR spectrum of He_N−OCS clusters between $N = 5$ and 6. For $N = 1-5$, a progressive blue shift was observed in the band origins. However, for $N > 5$, they turned around and began a steady red shift. This behavior could be explained by a "donut" model, in which the first five clustering He atoms assumed equivalent positions in a donut ring around the "equator" of the OCS molecule, close to the C atom, where they (evidently) have a blue-shifting effect on the C−O stretching vibration. After $N = 5$, there is no more room in the ring, so that the sixth and subsequent He atoms occupy positions closer to the ends of the OCS molecule, where they have a red-shifting effect on the vibration. We again know the limiting behavior for larger nanodroplets, where an overall red shift of -0.557 cm^{-1} has been observed[19] for the band origin.

For He_N−OCS clusters, the size range of $N \approx 9-11$ turns out to be difficult for a number of reasons. The infrared spectrum is particularly congested in the relevant spectral region, and for technical reasons, the microwave spectrometer is less sensitive in the important range for $R(0)$ lines (below or close to 3 GHz). Most importantly, the signals are weak for this size range. We believe that there actually are fewer clusters of this size in our apparatus, compared both to smaller and larger ones, an effect that must be due to the kinetics and energetics of cluster formation in the supersonic expansion. A similar effect around $N \approx 9$ has been noted[13] for He_N−CO_2 clusters. As a result of these difficulties, there remains a slight uncertainty (± 1) in our cluster size numbering above $N = 9$. However, for $N > 12$, the signals become strong again, and transitions can be confidently assigned with excellent agreement between the IR and MW data.

Infrared spectra showing cluster transitions for the size range $N \approx 12-20$ are shown in Figure 1. In this and other figures, the traces are arranged from bottom to top in order of increasing jet backing pressure (and sometimes decreasing jet temperature), so that the upper traces show increasingly larger clusters. The series that is assigned here to the $R(0)$ ($J = 1 \leftarrow 0$) transitions is particularly prominent for $N = 12-19$. There is an echo of this series at the left-hand side of Figure 1, and this can be assigned to the $P(1)$ transitions ($J = 0 \leftarrow 1$) belonging to the same cluster size range. Careful examination of the pressure dependence of the spectrum shows that the corresponding $R(1)$ ($J = 2 \leftarrow 1$) transitions are interleaved among the $R(0)$ series as indicated in Figure 1. The $R(0)$ series had been noted previously (see the asterisks in Figure 6 of ref 9), but the lines can now be assigned unambiguously (apart from the noted uncertainty of ± 1 in the absolute values of N) thanks to the improved spectral resolution offered by the skimmed jet and the availability of microwave data. For most of the clusters in this range, it was even possible to observe and assign the $R(2)$ and $P(2)$ IR transitions.

The frequencies of the $R(0)$ microwave transitions for $N = 12-20$ were calculated from the infrared data, and the transitions were found typically within 40 MHz of these initial predictions. The search for higher-J transitions was hampered by low signal strengths, and a double-resonance technique was used for their detection. In these experiments, the instrument was tuned to a known $R(0)$ ($J = 1 \leftarrow 0$) [or $R(1)$ ($J = 2 \leftarrow 1$)] transition, and the signal intensity was monitored as the pump radiation was scanned in successive experiments in 100 kHz increments. The inhomogeneous pump radiation field causes decoherence of the

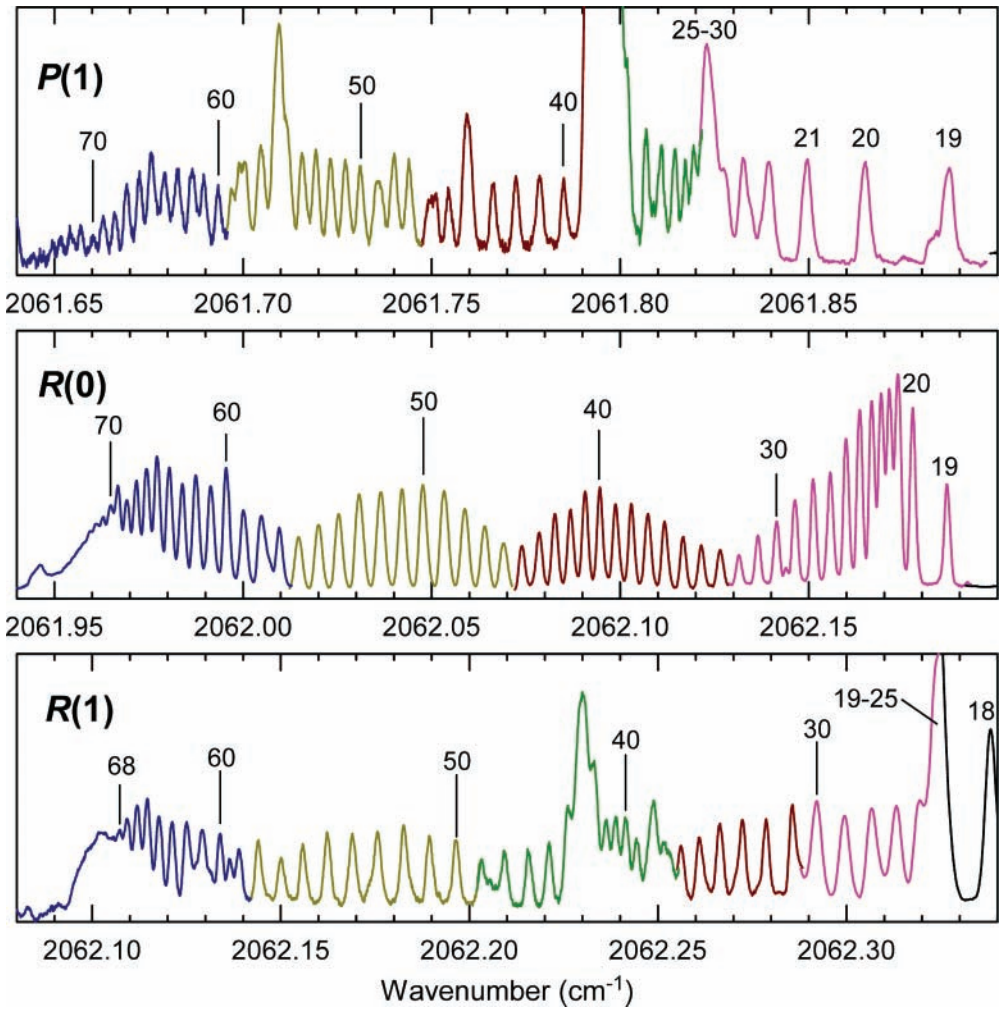

Figure 4. Observed IR spectra of He_N−OCS clusters, showing assigned cluster sizes, N, for the $P(1)$, $R(0)$, and $R(1)$ series. Each trace is a montage of five or six different spectra with experimental conditions varied to optimize the desired size ranges.

signal transition, and resonance of the pump frequency with the corresponding $R(1)$ ($J = 2 \leftarrow 1$) [or $R(2)$ ($J = 3 \leftarrow 2$)] transitions was detected as a significant decrease in signal intensity. Figure 2 shows an example of a double-resonance scan. This method is relatively narrow-banded, depending somewhat on the pump power, and it was possible to determine the pump transition frequencies to about 0.1 MHz. Up to $N = 18$, it was possible to subsequently record the $R(1)$ ($J = 2 \leftarrow 1$) pump transitions with higher precision in single-resonance experiments.

Table 1 lists the observed transitions for $11 < N < 21$. The assignments are rather secure for a number of reasons. The IR data are clear because the transitions are strong and well-separated, the MW $R(0)/R(1)$ pairs are linked by double resonance, and the MW and IR data agree extremely well when analyzed. This analysis is discussed below.

Returning to the size range of $N = 9-11$, the difficulties mentioned above are evident in Figure 1, where the relevant $R(0)$ transitions are not especially prominent in any of the traces shown. Because of the uncertainties, we do not wish to devote too much attention here to this range. However, some tentative assignments are given in Table 2. The transitions assigned to $N = 10$ are considered to be somewhat more satisfactory than those for $N = 9$ and 11. It is possible that there might be another unassigned cluster between those labeled $N = 9$ and 10 or that one cluster assigned here (e.g., $N = 11$) might not be real. These difficulties explain why we qualify our absolute size numberings for $N > 8$ with an uncertainty of ± 1.

3.2. He_N−OCS Clusters with $N > 20$. In the IR spectrum, a problem arises around $N = 20$ as the spacing between successive $R(0)$ transitions decreases and the transitions start to pile on top of each other. This pileup is illustrated in detail in Figure 3. Fortunately, by optimizing the instrumental resolution, it was possible to resolve and identify each individual transition. The closest spacing (0.002 cm^{-1}) occurs between $N = 22$ and 23, after which the line spacing increases slightly as N increases. Around the same point, the lines become weaker and never match the strength shown for $N \approx 14-19$. Similar but more serious pileups also occur in the $P(1)$ series at $N = 25-30$ and in the $R(1)$ series at $N = 19-25$. The pileups can be explained by the interplay between changing vibrational and rotational parameters, as will be seen below. To some extent, we could use spectral simulations to estimate the number of lines in these pileups. Fortunately, however, we did not have to rely solely on such simulations, as we also had MW data available to help "navigate" through the IR pileups.

It was possible to follow the microwave $R(0)$ series as it continued up in frequency from the values of 4462 and 4664 MHz observed for $N = 19$ and 20 (Table 1), by continuing to optimize experimental parameters (jet backing pressure and temperature). However, the $R(1)$ series was lost at this point. The loss can be explained partly by the increasing cluster B

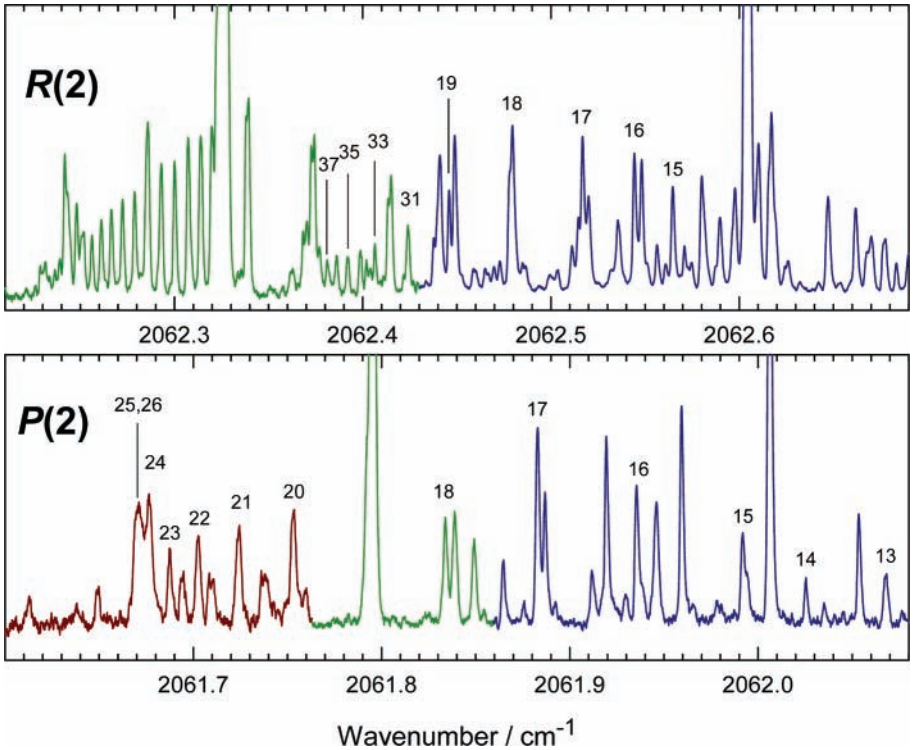

Figure 5. Observed IR spectra of the weak $P(2)$ and $R(2)$ series of He_N−OCS clusters, showing assigned cluster sizes, N. Each trace is a montage (see Figure 4).

values (which mean less population in the $J = 1$ level for a given cluster temperature) and partly by the difficult and time-consuming nature of searching for lines in FTMW spectroscopy, particularly when specific experimental conditions have to be maintained. In addition, the intensity of the microwave $R(0)$ series decreases with increasing N, and our double-resonance searches suffered from high noise levels. The MW $R(0)$ series continued to increase in frequency until it reached 5049 MHz for $N = 24$, and then it turned around. The transition frequencies decreased to a value of 4552 MHz at $N = 36$, and then the series turned around once more, reaching 4593 MHz at $N = 39$, the largest cluster that we detected in the MW region. As the experiments progressed, the IR and MW results were continually compared, with approximate IR predictions guiding the MW searches and precise MW observations verifying the IR assignments.

An overview of the observed $R(0)$, $P(1)$, and $R(1)$ IR transitions for $N > 20$ is shown in Figure 4. Each of these traces is a montage, with experimental conditions optimized for the particular size range. Remarkably, *all* of the $R(0)$ transitions for $N = 12-72$ were clearly observed. Beyond 72, the transitions become too closely spaced to resolve. The previously mentioned pileups of lines for $P(1)$ ($N = 25-30$) and for $R(1)$ (19−25) are visible here. Another tricky region occurs in the top trace of Figure 4 around 2061.8 cm^{-1} where the strong OCS monomer $P(1)$ line obscures the $P(1)$ series: fortunately, we could estimate positions by interpolation for the two missing lines with some confidence. Two further regions [at 2061.71 and 2062.23 cm^{-1} in the $P(1)$ and $R(1)$ series, respectively] are partly obscured by other transitions, but they posed no difficulty.

Some fragments of the much weaker $P(2)$ and $R(2)$ series were also observed, as shown in Figure 5. The $P(2)$ series follows from $N = 13-25$, with $N = 19$ obscured by the OCS monomer line at 2061.795 cm^{-1}. For $N = 25-35$, our analysis (see below) indicates that the $P(2)$ series piles up between 2161.65 and 2161.80 cm^{-1}, giving the unresolved lump apparent in the spectrum (lower trace of Figure 5). The $R(2)$ series transitions are assigned from $N = 15-19$, and the analysis indicates that there are then two turnarounds between $N = 20$ and $N = 29$, all falling in the range 2162.43−2162.48 cm^{-1} (some of these lines are very weakly visible between $N = 18$ and 19). The relative weakness of the $R(2)$ lines between $N = 20$ and $N = 29$ is understandable, as this coincides with a maximum in B (see below), meaning less population in the $J'' = 2$ initial state for a given temperature. Then, for $N = 30-37$, we were again able to assign the $R(2)$ transitions, before losing the series once more in a pileup of lines between 2162.37 and 2162.38 cm^{-1}. Incidentally, the beautiful array of lines around 2062.30 cm^{-1} in the upper trace of Figure 5 belongs to the $R(1)$ series (compare with Figure 4).

The observed IR and MW transitions of He_N−OCS clusters for $N = 9-20$ are reported in Tables 1 and 2, and a complete listing for $N = 12-72$ is provided in the Supporting Information. Figure 6 shows an overview of the line positions. For $N = 21-39$, there are three IR transitions, $R(0)$, $P(1)$, and $R(1)$, and one MW transition, $R(0)$. For $N = 40-68$, there are the three IR transitions, and for $N = 69-72$, there are the IR $R(0)$ and $P(1)$ lines. In the $P(1)$ and $R(1)$ IR series, there are regions where the line positions have to be interpolated, as discussed above.

3.3. He_N−OCS Clusters with $N > 72$. What about even larger clusters? These are indeed visible in the IR spectrum, but the individual lines are no longer resolved because the line spacing becomes too small. The situation is illustrated in Figure 7, where the top trace is a simulation of the observed nanodroplet spectrum of Grebenev et al.[19] and the other traces are our observed spectra with conditions favoring large clusters. In the center trace, which represents the most extreme clustering conditions achieved during the present study, the $R(1)$ transitions form a clear unresolved peak concentrated around 2062.094 cm^{-1}, and the $R(0)$ transitions form a strong peak at 2061.944 cm^{-1} with a subsidiary maximum around 2061.957 cm^{-1}. The $P(1)$ transitions are less prominent, and it appears that this might

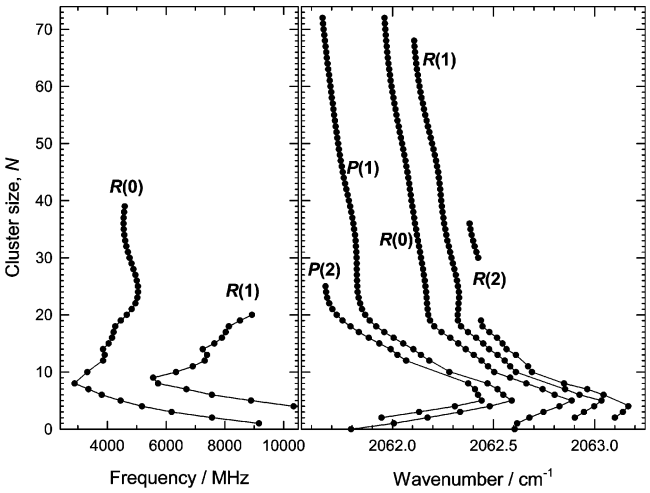

Figure 6. Overview of the measured MW (left-hand panel) and IR (right-hand panel) transitions of He_N−OCS clusters. Results for $N = 1-8$ are from refs 8 and 9.

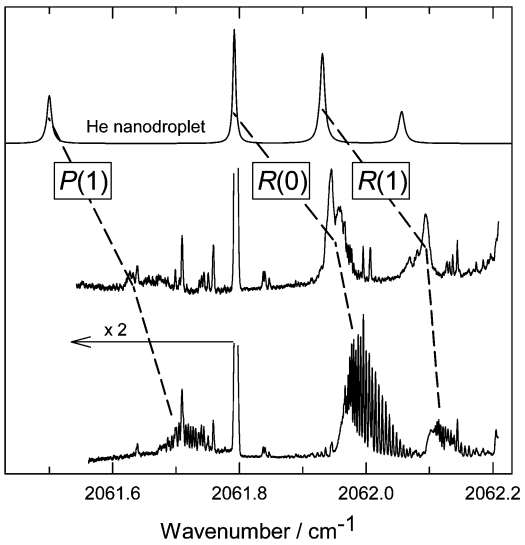

Figure 7. Observed IR spectra of larger He_N−OCS clusters (lower two traces) compared to a simulation of the observed[19] IR spectrum of OCS in He nanodroplets (top trace). The central trace probably corresponds to an average cluster size of $N \approx 100$. The strong feature at 2061.95 cm^{-1} in the lower two traces is an OCS molecule transition, but the line at almost the same position in the top trace is the real nanodroplet $R(0)$ transition.

be partly because they are more spread out than the R transitions. It is evident that the line positions in our largest clusters, with $N \approx 100$, are already within less than 0.2 cm^{-1} of their limiting nanodroplet values. Incidentally, note in Figure 7 that it is just by chance that the OCS monomer $P(1)$ line at 2061.795 cm^{-1} in the lower two traces is almost coincident with the nanodroplet $R(0)$ line[19] at 2061.792 cm^{-1} in the upper trace.

4. Analysis and Discussion

4.1. Linear Molecule Analysis. Each cluster size was analyzed in terms of a simple linear molecule (or $K = 0$ symmetric top) energy expression, with

$$E' = \nu_0 + B'J'(J'+1) - D\,[J'(J'+1)]^2$$

$$E'' = B''J''(J''+1) - D[J''(J''+1)]^2$$

where single and double primes refer to the excited and ground vibrational states, respectively. There were thus four adjustable parameters, the infrared band origin, ν_0; the upper- and lower-state rotational constants, B' and B''; and the centrifugal distortion constant, D, which was assumed to be equal for the upper and lower states. MW data were given a weight of 500 relative to IR data. (This weighting could be much higher if based on line measurement accuracy, but we felt the analysis was also limited by the applicability of the energy level model).

For $N = 12-20$, we had five to seven observed transitions and obtained very good fits to the data with the four-parameter model. One interesting result was that B' was consistently determined to be *larger* than B'', by an amount on the order of 0.0007 cm^{-1} (~20 MHz). At first, this was a slight surprise, as we know that the opposite holds true for the OCS monomer (and indeed for the stretching vibrations of most molecules) where normal anharmonicity results in $B' - B'' = -0.0012$ cm^{-1}. However, we quickly realized that it was known that $B' - B'' = +0.0012$ cm^{-1} for He nanodroplets[19] and that there was already a trend in this direction in our work on smaller He_N−OCS clusters with $N = 1-8$. The fact that $B' > B''$ for larger clusters might be due to changes in the He−OCS intermolecular potential (see section 4.2).

For $N = 21-39$, with a single MW transition and three or four IR transitions, the same trend continued, with very satisfactory fits and with the quantity $(B' - B'')$ settling down at values around $+0.0006$ cm^{-1}. Therefore, in the range of $N = 40-68$, with just three IR transitions available, it was decided to fix the quantity $(B' - B'')$ at an assumed value, which we (conservatively) took as $+0.0005$ cm^{-1}, or +15 MHz. Finally, for the range $N = 69-72$ with only two IR transitions, it was also necessary to fix D at an assumed value, which we took as the average of the values for the previous five clusters, 0.00061 cm^{-1}. The resulting parameters for He_N−OCS clusters are collected in Table 3 and also displayed in Figure 8.

4.2. Discussion of Derived Parameters. The observed variation of vibrational band origins with cluster size is shown in the top panel of Figure 8. The initial blue shift and turn around at $N = 5$ have already been discussed in terms of the model in which the first five He atoms occupy a ring around the equator of the OCS molecule, where each induces an increase in the vibrational frequency. Subsequent He atoms are then forced to locate closer to the ends of the OCS, where they induce a decrease in the frequency. The slight discontinuity in the band origin plot around $N = 9$ and 10 might be due to our problems in assigning the spectra in this region (see section 3.1). From the point of view of this curve, it seems that the assigned values of N might well be increased by 1 for $N > 10$. The problem with this conclusion, however, is that it would leave some missing clusters for which there are no viable MW and/or IR line assignments.

The dramatic change in slope of the band origin curve around $N = 19$ is associated with completion of the first solvation shell, after which each subsequent He atom has a much smaller effect on the OCS vibration. For $N > 20$, the curve smoothly settles down to a much reduced slope of about -0.004 cm^{-1} per added He atom. A broad and very slight upward bulge in the curve (roughly $N = 25-40$) might be an "echo" of the peak at $N = 5$, caused by the first atoms of the second solvation shell taking up positions around the equator of the OCS. At $N = 72$, the limiting nanodroplet value of the band origin is only about 0.16 cm^{-1} away, and the curve would reach this point by $N = 120$ if its slope remained constant. Yet, of course, it is very likely that the magnitude of the slope decreases further, and indeed, such a decrease is one of the reasons why the $R(0)$ lines in the IR spectrum are no longer resolved for $N > 72$.

TABLE 3: Fitted Parameters for He_N−OCS Clusters (in cm^{-1})[a]

N	ν_0	B'	B''	D
12	2062.3110	0.06548	0.06536	0.00054
13	2062.2709	0.06683	0.06641	0.00059
14	2062.2320	0.06631	0.06556	0.00064
15	2062.1885	0.06960	0.06869	0.00062
16	2062.1449	0.07144	0.07055	0.00058
17	2062.1001	0.07227	0.07135	0.00055
18	2062.0623	0.07323	0.07235	0.00056
19	2062.0361	0.07621	0.07555	0.00056
20	2062.0207	0.07956	0.07891	0.00056
21	2062.0106	0.08257	0.08167	0.00053
22	2062.0050	0.08413	0.08357	0.00048
23	2062.0000	0.08548	0.08464	0.00044
24	2061.9965	0.08590	0.08504	0.00042
25	2061.9940	0.08552	0.08487	0.00041
26	2061.9916	0.08486	0.08428	0.00040
27	2061.9890	0.08421	0.08349	0.00044
28	2061.9864	0.08327	0.08247	0.00045
29	2061.9840	0.08213	0.08138	0.00045
30	2061.9813	0.08103	0.08031	0.00046
31	2061.9784	0.07992	0.07927	0.00044
32	2061.9750	0.07906	0.07842	0.00044
33	2061.9715	0.07835	0.07775	0.00045
34	2061.9674	0.07781	0.07721	0.00043
35	2061.9629	0.07768	0.07692	0.00044
36	2061.9586	0.07730	0.07673	0.00040
37	2061.9541	0.07733	0.07678	0.00039
38	2061.9492	0.07760	0.07703	0.00040
39	2061.9442	0.07797	0.07741	0.00040
40	2061.9391	0.07846	0.07796	0.00039
41	2061.9340	0.07901	0.07851	0.00038
42	2061.9288	0.07964	0.07914	0.00038
43	2061.9237	0.08020	0.07970	0.00039
44	2061.9185	0.08075	0.08025	0.00040
45	2061.9137	0.08090	0.08040	0.00039
46	2061.9089	0.08103	0.08053	0.00040
47	2061.9037	0.08112	0.08062	0.00042
48	2061.8988	0.08093	0.08043	0.00044
49	2061.8939	0.08066	0.08016	0.00044
50	2061.8889	0.08040	0.07990	0.00048
51	2061.8842	0.08006	0.07956	0.00050
52	2061.8793	0.07954	0.07904	0.00050
53	2061.8746	0.07914	0.07864	0.00052
54	2061.8700	0.07878	0.07828	0.00054
55	2061.8654	0.07851	0.07801	0.00057
56	2061.8611	0.07800	0.07750	0.00056
57	2061.8566	0.07754	0.07704	0.00055
58	2061.8521	0.07743	0.07693	0.00059
59	2061.8480	0.07712	0.07662	0.00058
60	2061.8440	0.07685	0.07635	0.00058
61	2061.8399	0.07681	0.07631	0.00059
62	2061.8365	0.07667	0.07617	0.00060
63	2061.8328	0.07671	0.07621	0.00060
64	2061.8293	0.07677	0.07627	0.00061
65	2061.8259	0.07685	0.07635	0.00061
66	2061.8229	0.07692	0.07642	0.00061
67	2061.8200	0.07708	0.07658	0.00063
68	2061.8172	0.07724	0.07674	0.00062
69	2061.8145	0.07750	0.07700	0.00061
70	2061.8119	0.07774	0.07724	0.00061
71	2061.8093	0.07790	0.07740	0.00061
72	2061.8070	0.07814	0.07764	0.00061
nanodroplet[b]	2061.644	0.0744	0.0732	0.00038

[a] For $N = 40-72$, $(B' - B'')$ was fixed at $+0.0005$ cm^{-1}; for $N = 69-72$, D was fixed at 0.00061 cm^{-1} (see text). [b] From Grebenev et al.[19]

The plot of B values in the central panel of Figure 8 illustrates one of the most interesting and unexpected results of this work. Following the initial drop in B ($N = 1-9$), there is a turn around as superfluid effects become significant, and some of the He atoms decouple from the OCS rotational motion. The slight kink at $N = 14$ is real and might be evidence of a structural rearrangement at this point; similar but more pronounced effects were observed[14] for He_N−N_2O clusters in the same size range. The B values continue rising, through a slight hesitation ($N = 16-18$) that might mark completion of the first solvation shell, to a broad maximum centered at $N = 24$. At this point, the B value (0.085 cm^{-1}) lies significantly above its nanodroplet limit (0.073 cm^{-1}). The gradual decrease of B toward this limit is modulated by broad oscillations with maxima at $N = 24$ and 47 and minima at $N = 36$ and 62. There must be at least one further maximum in the curve because the B values are rising at $N = 72$. Furthermore, the presence of continuing oscillations for $N > 100$ is suggested by the double-peaked shape of the unresolved $R(0)$ feature in the central trace of Figure 7 [the peaks would coincide with the bunching together of $R(0)$ lines as rising B values oppose some of the effect of falling band origins]. There have been a number of calculations[23−27] of B values of for He_N−OCS clusters in this size range (see Figure 2 of ref 33), but none have indicated this oscillatory behavior.

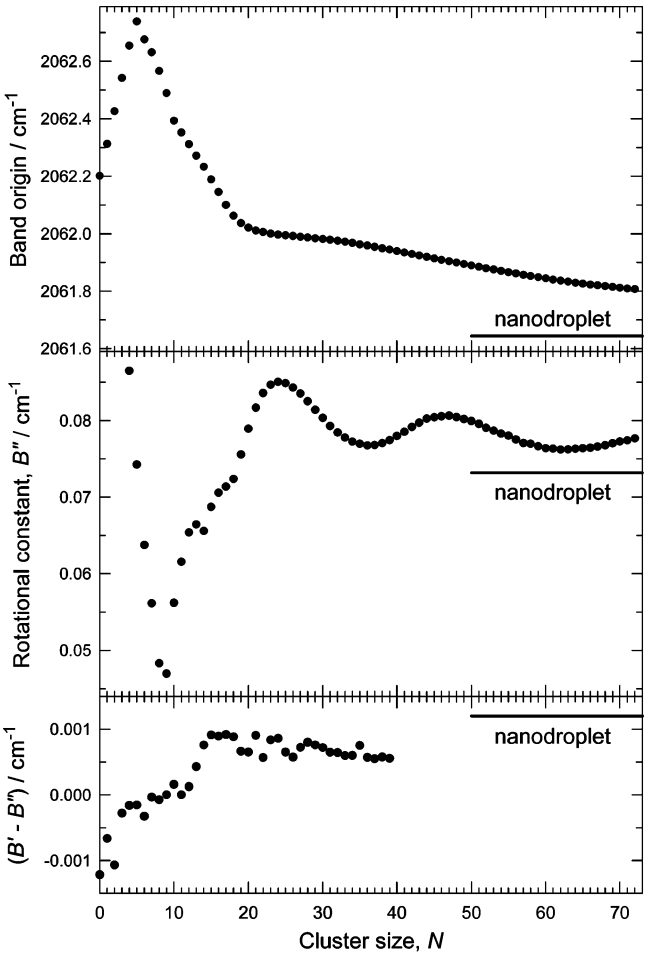

Figure 8. Variation with cluster size of the IR band origin, ν_0 (top panel); the ground-state rotational constant, B'' (middle panel); and the vibrational change in rotational constant, $B' - B''$ (bottom panel). Results for $N = 1-8$ from refs 8 and 9. Limiting nanodroplet values from ref 19 are shown as horizontal lines.

The lower panel of Figure 8 shows the variation of $B' - B''$, the difference in B values between the excited and ground vibrational states. For the OCS molecule and the smaller clusters ($N = 1$ and 2), this difference is negative, because OCS itself is slightly longer when vibrationally excited, because of anharmonicity. However, with increasing cluster size, the difference moves close to 0, becoming positive for $N > 12$. At $N = 15$, it is equal to $+0.0009$ cm^{-1}, already close to the nanodroplet value of $+0.0012$ cm^{-1}. We believe that the positive

sign of $B' - B''$ for larger clusters is an indication that the effective angular anisotropy in the OCS−He intermolecular potential is slightly smaller in the excited vibrational state, thus allowing the OCS molecule to rotate slightly more freely. This supposition is consistent with the observed blue shift of the IR band origin for clusters with $N = 1-5$, as this shows directly that the deepest part of the intermolecular potential (where the first five He atoms are located) becomes less deep upon vibrational excitation. It is also indicated by the most recent OCS−He ab initio potential, for which the difference between lowest and highest points in the minimum-energy angular path was calculated to be slightly less in the excited vibrational state (33.72 vs 34.16 cm^{-1}).[25]

The observed values (Table 3) of the centrifugal distortion parameter, D, fall around 0.0006 cm^{-1} for $N = 12$ and 70 and drop slightly to around 0.0004 cm^{-1} for intermediate sizes, $N \approx 20-50$. This range for D is not very different from the nanodroplet value,[19] 0.00038 cm^{-1}, showing again (as with $B' - B''$ and B itself) that the rotational motion of OCS in small He clusters (i.e., $N \approx 20$) is in some sense already similar to that in nanodroplets.

5. Conclusions

We believe that the observed broad oscillations in the B value (and hence in the effective inverse moment of inertia) constitute evidence for some sort of evolving solvation shell structure, an aufbau ("building up") of superfluid He atoms around the OCS molecule.[33] However, the connection of this shell structure with the "real" structural shells is not as clear, given that the conventional expectation is for the first and second solvation shells to be filled around $N \approx 18$ and 70, respectively. In other words, we seem to observe two full oscillation cycles during filling of the second shell. Andrey Vilesov[37] has pointed out to us a possible analogy in measurements of the third sound velocity for ^{4}He films on solid H_2, where two oscillation cycles were also observed per helium layer.[38] As well, Vilesov suggests that our oscillations could reflect a coupling between rotation and cluster surface excitations. As the energy of a particular excitation mode passes through a local maximum, its coupling with the OCS rotation will be minimized, and a peak in B would be expected. This has been calculated[39] to occur around $N \approx 50$ for the dominant quadrupole excitation in He clusters doped with SF_6 and could help to explain our observed maximum in B at $N = 47$.

In conclusion, we wish to emphasize three significant aspects of the present work. The first is the observation of broad oscillations in the rotational constant, B. This behavior had not been anticipated, and it raises challenges for theoretical simulations: first to reproduce the effect and then to explain it. A second significant observation is that it appears relatively easy to produce fairly narrow size distributions of cold (0.2 K) medium-sized doped helium clusters in seeded supersonic jets. For example, the central trace in Figure 3 and the lower trace in Figure 7 show average cluster sizes of $N \approx 20$ and 60, together with widths of $\Delta N \approx 7$ and 14. We wonder if such seeded jets could provide an interesting complement to the usual techniques used in helium nanodroplet experiments (i.e., pure He jet followed by pickup cells). The third significant aspect of our work is that sharp (instrument-limited) lines were observed even for the largest clusters studied. The fact that microwave transitions with $\Delta\nu \approx 15$ kHz were observed for clusters with $N = 39$ (and infrared transitions with $\Delta\nu \approx 0.001$ cm^{-1} for $N = 72$) is remarkable in itself. However, it also has implications for our understanding of broadening effects in nanodroplets, and it has the potential to open up a new range of precision spectroscopic experiments on medium-size helium clusters at very low temperatures.

Acknowledgment. This work was supported by the Natural Sciences and Engineering Research Council of Canada and the National Research Council of Canada. We are grateful to A. Vilesov, N. Blinov, P.-N. Roy, and J. K. G. Watson for stimulating discussions and to H. Mäder for insights into the decoherence double-resonance technique.

Supporting Information Available: Listings of the observed IR (Table A-1) and MW (Table A-2) transitions and calculated values based on the parameters of Table 3. This material is available free of charge via the Internet at http://pubs.acs.org.

References and Notes

(1) Callegari, C.; Lehmann, K. K.; Schmied, R.; Scoles, G. *J. Chem. Phys.* **2001**, *115*, 10090−10110.
(2) Toennies, J. P.; Vilesov, A. F. *Angew. Chem., Int. Ed.* **2004**, *43*, 2622−2648.
(3) Barranco, M.; Guardiola, R.; Hernández, S.; Mayol, R.; Navarro, J.; Pi, M. *J. Low Temp. Phys.* **2006**, *142*, 1−81.
(4) Choi, M. Y.; Douberly, G. E.; Falconer, T. M.; Lewis, W. K.; Lindsay, C. M.; Merritt, J. M.; Stiles, P. L.; Miller, R. E. *Int. Rev. Phys. Chem.* **2006**, *25*, 15−75.
(5) Grebenev, S.; Toennies, J. P.; Vilesov, A. F. *Science* **1998**, *279*, 2083−2086.
(6) Andronikashvili, E. L. *J. Phys. U.S.S.R.* **1946**, *10*, 201−206.
(7) Tang, J.; Xu, Y.; McKellar, A. R. W.; Jäger, W. *Science* **2002**, *297*, 2030−2033.
(8) Xu, Y.; Jäger, W. *J. Chem. Phys.* **2003**, *119*, 5457−5466.
(9) Tang, J.; McKellar, A. R. W. *J. Chem. Phys.* **2003**, *119*, 5467−5477.
(10) Abusara, Z.; Borvayeh, L.; Moazzen-Ahmadi, N.; McKellar, A. R. W. *J. Chem. Phys.* **2006**, *125*, 144307.
(11) Xu, Y.; Jäger, W.; Tang, J.; McKellar, A. R. W. *Phys. Rev. Lett.* **2003**, *91*, 163401.
(12) Tang, J.; McKellar, A. R. W.; Mezzacapo, F.; Moroni, S. *Phys. Rev. Lett.* **2004**, *92*, 145503.
(13) Tang, J.; McKellar, A. R. W. *J. Chem. Phys.* **2004**, *121*, 181−190.
(14) Xu, Y.; Blinov, N.; Roy, P.-N.; Jäger, W. *J. Chem. Phys.* **2006**, *124*, 081101.
(15) Topic, W.; Jäger, W.; Blinov, N.; Roy, P.-N.; Botti, M.; Moroni, S. *J. Chem. Phys.* **2006**, *125*, 144310.
(16) Tang, J.; McKellar, A. R. W. *J. Chem. Phys.* **2003**, *119*, 754−764.
(17) Tang, J.; McKellar, A. R. W. *J. Chem. Phys.* **2004**, *121*, 6868−6873.
(18) McKellar, A. R. W. *J. Chem. Phys.* **2006**, *125*, 164328.
(19) Grebenev, S.; Hartmann, M.; Havenith, M.; Sartakov, B.; Toennies, J. P.; Vilesov, A. F. *J. Chem. Phys.* **2000**, *112*, 4485−4495.
(20) Grebenev, S.; Havenith, M.; Madeja, F.; Toennies, J. P.; Vilesov, A. F. *J. Chem. Phys.* **2000**, *113*, 9060−9066.
(21) Kunze, M.; Markwick, P. R. L.; Pörtner, N.; Reuss, J.; Havenith, M. *J. Chem. Phys.* **2002**, *116*, 7473−7485.
(22) Paesani, F.; Gianturco, F. A.; Whaley, K. B. *J. Chem. Phys.* **2001**, *115*, 10225−10238.
(23) Paesani, F.; Viel, A.; Gianturco, F. A.; Whaley, K. B. *Phys. Rev. Lett.* **2003**, *90*, 073401.
(24) Moroni, S.; Sarsa, A.; Fantoni, S.; Schmidt, K. E.; Baroni, S. *Phys. Rev. Lett.* **2003**, *90*, 143401.
(25) Paesani, F.; Whaley, K. B. *J. Chem. Phys.* **2004**, *121*, 4180−4192.
(26) Zillich, R.; Paesani, F.; Kwon, Y.; Whaley, K. B. *J. Chem. Phys.* **2005**, *123*, 114301.
(27) Paolini, S.; Fantoni, S.; Moroni, S.; Baroni, S. *J. Chem. Phys.* **2005**, *123*, 114306.
(28) Gianturco, F. A.; Paesani, F. *J. Chem. Phys.* **2000**, *113*, 3011−3019.
(29) Howson, J. M. M.; Hutson, J. M. *J. Chem. Phys.* **2001**, *115*, 5059−5065.
(30) Higgins, K.; Klemperer, W. *J. Chem. Phys.* **1999**, *110*, 1383−1388.
(31) Tang, J.; McKellar, A. R. W. *J. Chem. Phys.* **2001**, *115*, 3053−3056.
(32) Tang, J.; McKellar, A. R. W. *J. Chem. Phys.* **2002**, *117*, 2586−2591.

(33) McKellar, A. R. W.; Xu, Y.; Jäger, W. *Phys. Rev. Lett.* **2006**, *97*, 183401.
(34) Brookes, M. D.; Xia, C.; Tang, J.; Anstey, J. A.; Fulsom, B. G.; Au Yong, K.-X.; King, J. M.; McKellar, A. R. W. *Spectrochim. Acta A* **2004**, *60*, 3235−3241.
(35) Xu, Y.; Jäger, W. *J. Chem. Phys.* **1997**, *106*, 7968−7980.
(36) Markov, V. N.; Xu, Y.; Jäger, W. *Rev. Sci. Instrum.* **1998**, *69*, 4061−4067.
(37) Vilesov, A. Private communication, 2006.
(38) Shirron, P. J.; Mochel, J. M. *Phys. Rev. Lett.* **1991**, *67*, 1118−1121.
(39) Chin, S. A.; Krotscheck, E. *Phys. Rev. B* **1995**, *52*, 10405−10428.